GEOPHYSICS. VOL. 77, NO. 1 (JANUARY-FEBRUARY 2012); P. 1–14, 12 FIGS., 1 TABLE.
10.1190/GEO2010-0129.1

Mapping the magnetic susceptibility and electric conductivity of marine surficial sediments by benthic EM profiling

Hendrik Müller[1], Tilo von Dobeneck[1], Christian Hilgenfeldt[1], Bill SanFilipo[2], Daniel Rey[3], and Belén Rubio[3]

ABSTRACT

Distribution, accumulation, and diagenesis of surficial sediments in coastal and continental shelf systems follow complex chains of localized processes and form deposits of great spatial variability. Given the environmental and economic relevance of ocean margins, there is growing need for innovative geophysical exploration methods to characterize seafloor sediments by more than acoustic properties. A newly conceptualized benthic profiling and data processing approach based on controlled-source electromagnetic (CSEM) imaging permits to coevally quantify the magnetic susceptibility and the electric conductivity of shallow marine deposits. The two physical properties differ fundamentally insofar as magnetic susceptibility mostly assesses solid particle characteristics such as terrigenous or iron mineral content, redox state, and contamination level, while electric conductivity primarily relates to the fluid-filled pore space and detects salinity, porosity, and grain-size variations. We develop and validate a layered half-space inversion algorithm for submarine multifrequency CSEM with concentric sensor configuration. Guided by results of modeling, we modified a commercial land CSEM sensor for submarine application, which was mounted into a nonconductive and nonmagnetic bottom-towed sled. This benthic EM profiler *Neridis II* achieves 25 soundings/second at 3–4 knots over continuous profiles of up to a hundred kilometers. Magnetic susceptibility is determined from the 75 Hz in-phase response (90% signal originates from the top 50 cm), while electric conductivity is derived from the 5 kHz out-of-phase (quadrature) component (90% signal from the top 92 cm). Exemplary survey data from the north-west Iberian margin underline the excellent sensitivity, functionality, and robustness of the system in littoral (~0–50 m) and neritic (~50–300 m) environments. Susceptibility versus porosity crossplots successfully identify known lithofacies units and their transitions. All presently available data indicate an eminent potential of CSEM profiling for assessing the complex distribution of shallow marine surficial sediments and for revealing climatic, hydrodynamic, diagenetic, and anthropogenic factors governing their formation.

INTRODUCTION

Coastal and continental shelf sedimentary systems are complex interim deposits in the transport chain from land to ocean. Storage and release, production, and alteration of sediment particles at and near the seafloor depend on their physical and chemical material properties and the local impact of waves, currents, tides, tectonics, biota, gas, and fluid seepage. The very dynamic nature of shallow marine settings finds its geological expression in vast lateral variability and frequent discontinuity of the sedimentary bodies. Human impact by trawling, mining, dredging, dumping, and offshore construction plays an increasing role in modifying transport patterns and subsequently sediment distribution and benthic environment. An improved understanding of sediment dynamics under growing anthropogenic pressure is of paramount importance for integrated coastal zone management (ICZM) to hold the balance of environmental and economic interests. In particular, the precise knowledge of the near-surface architecture of coastal and shelf sediments, including quantitative high-resolution data on the composition,

Manuscript received by the Editor 28 April 2010; revised manuscript received 28 June 2011.
[1]MARUM — Center for Marine Environmental Sciences and Faculty of Geosciences, University of Bremen, Bremen, Germany. E-mail: hendrik.mueller@uni-bremen.de; dobeneck@uni-bremen.de; chilgenfeldt@uni-bremen.de.
[2]Geophex Ltd., Raleigh, North Carolina (deceased), USA.
[3]Universidad de Vigo, Departamento de Geociencias Marinas, Vigo, Spain. E-mail: danirey@uvigo.es; brubio@uvigo.es.

porosity, texture, as well as mechanical and chemical properties of the seafloor will be instrumental.

Geophysical exploration methods can provide the lateral resolution, the vertical penetration, and parameterization required to image sedimentary patterns in their full spatial complexity. In particular sidescan sonars, single- and multibeam echosounders, and multichannel seismic reflection methods have been intensely used in this context (e.g., Yilmaz, 1987; Kenny et al., 2003). These methods excel in resolving bottom topography and subbottom stratification, but are limited and often ambiguous when it comes to determining sediment properties (e.g., grain-size, porosity, mineralogy) or to map surface heterogeneities. As shown, e.g., by Evans (2001), electromagnetic imaging of seafloor resistivity is a promising method to gather quantitative information on sediment porosity, an expression of grain-size and consolidation. Radiometric mapping of seafloor radionuclides (K, U, Th) is an alternative approach capable of discerning mud and sands from various provenances (De Meijer et al., 1996; van Wijngaarden et al., 2002).

Magnetic properties of shallow marine sediments have also been exploited in shallow marine studies, but mainly on collected samples. Magnetic trace minerals, especially iron-oxides, have source-specific rock magnetic and elemental signatures that can be detected by mineral and grain-size specific bulk measurements. The environmental specificity and available instrumental sensitivity of laboratory rock magnetic analytics lends iron-oxides an excellent potential as markers of sediment provenances, transport, diagenesis, and environmental quality in coastal and continental shelf systems (Zhang et al., 2001; Tribovillard et al., 2002; Emiroglu et al., 2004; Rey et al., 2005; Ellwood et al., 2006; Maher et al., 2009; Mohamed et al., 2010). Owing to its commonly fine crystal size in magmatic rocks, detrital (titano-)magnetite tends to enrich in the fine fraction of sediments, providing a means to quantify terrigenous clay and silt content from bulk magnetic susceptibility measurements (Oldfield et al., 1985; Booth et al., 2005; Ellwood et al., 2006; Hatfield and Maher, 2009).

In spite of the promises of using magnetic susceptibility measurements in the mapping of shallow marine sediment distribution, the step from sample-based to in situ measurement has not been taken because of inherent instrumental difficulties. Due to strong inductive effects, standard alternating field susceptometers (e.g., Bartington MS2 type) do not operate properly in the highly conductive marine environment (Benech and Marmet, 1999). Passive marine (seasurface or deep-towed) magnetometry can only detect relatively sharp lateral magnetization contrasts and does not resolve the subtle magnetic variability of surficial sediments, especially in presence of magnetically more prominent deeper geological structures (Gay, 2004).

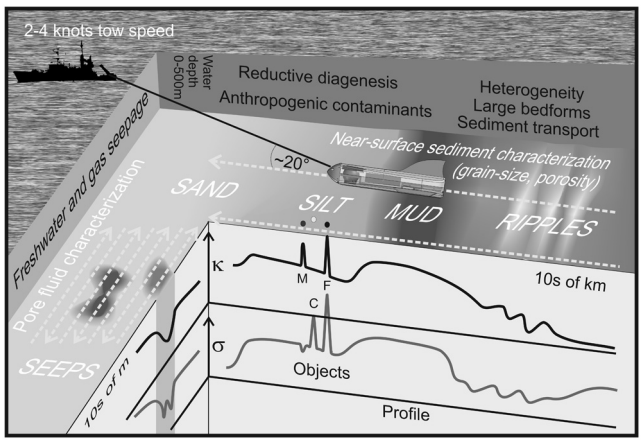

Figure 1. Conceptual model of benthic EM profiling and mapping. Surficial sediments, freshwater seeps, and objects (M: magnetic, C: conductive, F: ferrous) can be identified by their electric conductivity σ and magnetic susceptibility κ signatures.

The best available technology for submarine susceptometry is controlled-source electromagnetics (CSEM). The magnetic susceptibility κ and electric conductivity σ of marine surficial sediments can be separately determined from low and high transmitter frequencies and an independent measurement of ambient seawater conductivity. This concept was realized with the new bottom-towed benthic profiler *Neridis II* (NERItic DIScoverer; Figure 1), which we developed in close cooperation of the MARUM Center for Marine Environmental Sciences at the University of Bremen (Germany) and the GEOMA Marine and Environmental Geology Group at the University of Vigo (Spain). This system uses a commercial frequency domain CSEM sensor (Won et al., 1997) and is devised for coastal and continental shelf operations down to 500 m water depth, targeting essentially the topmost 50 cm of the subseafloor.

For the purpose of mapping shallow marine sediment characteristics, seepage effects, and metallic contaminants, it is essential to consider the spatial variability of the solid particles (here defined as sediment matrix), as well as of the (fluid-filled) pore space. The two parameters κ and σ derived from CSEM provide just that: the magnetic susceptibility of sediment depends on its ferro-, para-, and diamagnetic mineral content, hence on lithology and grain-size. The electric conductivity of marine sediments is determined by their pore water salinity, porosity, temperature, and clay content. Porosity depends on the granular packing structure and is controlled by grain-size and shape, sorting, and compaction level (e.g., Jackson et al., 1978). As the conceptual κ and σ profiles of Figure 1 suggest, both parameters offer to some degree related, but also complementary information on various primary and secondary geological processes. Results of a high-resolution survey of freshwater seeps in Eckernförde Bay (SW Baltic Sea) have been published separately (Müller et al., 2011). Therein, we demonstrate that EM profiling, complemented and validated by acoustic, as well as sample-based rock magnetic and geochemical methods, can create a crisp and revealing fingerprint image of freshwater seepage and reductive alteration of near-surface sediments.

This paper presents physical principles, technical realization, and first successful scientific applications of the new benthic EM profiler. In particular, we will discuss

- implications of the sensor geometry,
- impact of the conductive saltwater environment,
- lithologic and morphologic controls of susceptibility and conductivity,
- design and operation of the bottom-towed system.

Two 33 and 19 km long crossprofiles of the northwest Iberian continental shelf will be used to illustrate the applicability of this novel seafloor mapping tool and highlight the eminent potential of combining magnetic and electric information for quantitative seabed characterization.

EM MEASUREMENTS IN A CONDUCTIVE SALTWATER ENVIRONMENT

So far, most CSEM-based studies of marine sediments have been exclusively interested in subsurface conductivity, and there is a range of publications addressing the problems created by the influence of the conductive saltwater environment (e.g., Cheesman et al., 1987; Chave et al., 1991; Edwards, 2005). Specific constraints must be met by sensor type and geometry to measure subsurface conductivity without a priori knowledge of seawater conductivity (e.g., Cheesman et al., 1987). Especially in shallow waters, the EM subsurface signal can be significantly biased by effects related to the air-water boundary, current driven water turbulences, and wave motion (Chave et al., 1991; Manoj et al., 2006). Due to the damping of the EM signal in the water column, sensitive EM measurements must be performed close to the seafloor where obstacles of various types (e.g., ship wrecks, rocks, terraces, cables, fishing gear) hold risks for the instrumentation and survey success. Some benefit is provided by low-pass filtering of cultural noise and spherics by the conductive seawater drape (Chave et al., 1991).

Primary and secondary EM signal

EM field instruments capable of measuring magnetic susceptibility differ fundamentally by the arrangement of transmitter and receiver coil (Benech and Marmet, 1999). "Slingram" type or bistatic sensor geometries, where the receiver coil is apart from the transmitter coil, enable greater depths of investigation and are less influenced by a conductive subsurface. However, they are much less sensitive for susceptibility and, therefore, not useful for the earlier depicted purpose, where precisions in the order of 10^{-6} (dimensionless SI-units) are required. As the magnetic dipole-field decays by the inverse cube of the distance, the highest amplitude of the secondary magnetic field due to a magnetized body is detected by a receiver loop, which is concentric and coplanar with the transmitter coil. The commercial broadband CSEM sensor GEM-3 (Won et al., 1997) applies this principle and is capable of separating magnetic susceptibility and electric conductivity by combining low- and high-frequency signals (Won and Huang, 2004). Its sensitivity for magnetic susceptibility was determined as 7×10^{-7} in a low noise environment at 5 Hz sampling rate. The base period of the transmitter waveform is 25 Hz (30 Hz in 60 Hz power environment), which defines the minimum operation frequency and maximum sampling rate. Up to ten frequencies of 25 Hz to 50 kHz can be combined to build a complex waveform using a pulse-width modulation technique (Won et al., 1996).

An outstanding advantage of the GEM-3 sensor is due to the technique it employs for "bucking" the magnetic source field of the transmitter coil T_x (∅ 96 cm) at the receiver coil R_x (∅ 30 cm). This is realized by adding a third, equally concentric "bucking coil" B_x (∅ 53 cm) in series with the transmitter coil, but with reverse winding and half number of turns. The bucking coil is tuned such that it cancels the transmitter moment within a central magnetic cavity area by its corresponding, but inverse signal (Figure 2a). Ideally, the receiver coil does not see the primary transmitter signal and therefore only registers the secondary subsurface response.

Due to the interference of transmitter and bucking field, the primary field in the sensor plane changes polarity at the positions of T_x and B_x and approaches zero inside R_x (Figure 2a and 2b; both figure parts were computed using a finite-element model). The full-space (air or seawater) image of the primary magnetic field (Figure 2b) demonstrates that an inverse polarization due to the B_x field predominates up to a vertical distance of 20 cm. At greater depth, positive polarity of the transmitter coil starts to dominate the

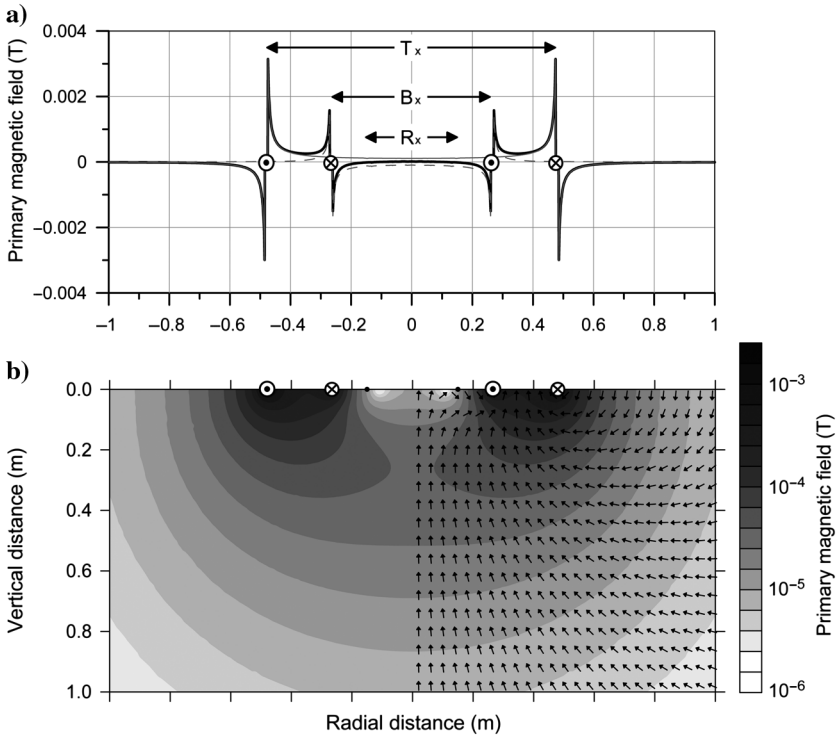

Figure 2. Primary magnetic field intensity distribution of EM sensor in (a) sensor plane (*thin gray line*: transmitter coil field, *dashed gray line*: bucking coil field, *thick black line*: total field) and (b) vertical cross section. Vectors indicate field directions; dots represent the positions of transmitter (T_x), bucking (B_x) and receiver (R_x) coil and momentary sense of the alternating primary current (both figure parts were computed using a COMSOL Multiphysics finite-element model).

primary field and a dipolar characteristic can be assumed at depths greater than 40 cm. In consequence of the primary and resulting secondary field geometries, the total sensitivity of the sensor reaches its maximum when the sensor is placed 20 cm above the ground. This defines the optimum elevation for seafloor sediment measurements, where the region affected by the bucking field is situated within nearly homogeneous seawater.

To understand the fundamentals of the received signal, we expand the analytical half-space equation of the GEM-3 sensor for a conductive upper half-space and a magnetic subsurface (see appendix A). The sensor output is defined as the ratio of the secondary magnetic field normalized to the primary magnetic field in absence of the bucking coil, both measured by the receiver coil (Won et al., 1997). This complex ratio U is given in a dimensionless unit of parts-per-million (ppm) and has a real (in-phase) and an imaginary (out-of-phase or quadrature) component, expressed in the radial symmetric *receiver function*:

$$U = \frac{2R_t^2}{R_r} \cdot \int_0^\infty G \cdot \frac{\lambda}{u_w} \cdot e^{-2u_w h} \cdot \left[\frac{\mu_s u_w - \mu_w u_s}{\mu_s u_w + \mu_w u_s}\right] \mathrm{d}\lambda + \frac{2R_t^2}{R_r} \cdot \int_0^\infty G \cdot \left[\frac{\lambda}{u_w} - 1\right] \mathrm{d}\lambda$$

$$\text{where} \quad G = \left[J_1(\lambda R_T) - \frac{n_b R_b}{n_t R_t} J_1(\lambda R_b)\right] J_1(\lambda R_r)$$

$$\text{and} \quad u_w = \sqrt{\lambda^2 + i\omega\mu_0\mu_w\sigma_w},$$

$$u_s = \sqrt{\lambda^2 + i\omega\mu_0\mu_s\sigma_s} \tag{1}$$

with sediment respective seawater electric conductivity σ_s, σ_w (s: sediment, w: seawater), constant of integration λ, relative magnetic permeability μ_s, μ_w (magnetic susceptibility $\kappa = \mu - 1$), magnetic permeability μ_0 of free space, Bessel function of first kind and order J_1, imaginary number i, angular frequency ω ($\omega = 2\pi f$; f: frequency), sensor elevation h, receiver coil radius R_r, transmitter coil radius R_t, bucking coil radius R_b and number of respective coil turns n_t and n_b. In practice, the transmitter field is directly measured by a small reference coil, located in the sensor plane between the bucking and transmitter coil (at a radius of approximately 40 cm in Figure 2a, where $B_x \approx 0$) and multiplied by a geometric scaling factor. Seawater conductivity σ_w is determined with an oceanographic conductivity-temperature-depth (CTD) probe, which is mounted inside the Neridis II benthic profiler. As the diamagnetic susceptibility of seawater κ_w is a temperature-independent constant, a value of -9×10^{-6} (Collinson, 1983) is assumed.

Low frequency expansion of the receiver function (equation 1) represents the "resistive limit" conditions, where the conductive seawater and subseafloor behave like a perfect resistor. Thus, the primary and the secondary field are in phase (real) and seawater and subsurface conductivity effects can be neglected. Under these conditions, the secondary signal is proportional to the magnetic susceptibility κ_s and the receiver function (equation 1) can be approximated by the *resistive limit equation* where seawater susceptibility is neglected ($\mu_w \approx 1$)

$$U = \frac{2R_t^2}{R_r} \int_0^\infty G \cdot r_{TE} e^{-2\lambda h} \mathrm{d}\lambda = \kappa_s \cdot \frac{R_t^2}{R_r} \int_0^\infty G \cdot e^{-2\lambda h} \mathrm{d}\lambda,$$

$$\text{where} \quad r_{TE} = \frac{\mu_s - 1}{\mu_s + 1} = \frac{\kappa_s}{\kappa_s + 2} \approx \frac{\kappa_s}{2}, \ \text{as} \ \kappa_s \ll 2. \tag{2}$$

Frequency dependence of the susceptibility signal can arise from superparamagnetic magnetite (Buselli, 1982; Dearing et al., 1996) or subsurface magnetization by secondary EM fields (Zhang and Oldenburg, 1997). However, the currents induced by this system in marine sediments will usually not exceed 1 A, and thus a maximum secondary magnetic field is <1 μT, which is at least two orders of magnitude lower than the primary magnetic field. Hence, more than 99% of the measured magnetic susceptibility is related to primary EM field magnetization.

Sediment electric conductivity σ_s is commonly interpreted as a measure of (connected) porosity. The empirical relation of sediment conductivity, pore water conductivity σ_w and porosity ϕ is given by Archie's law (Archie, 1942):

$$\sigma_s = a \cdot \sigma_w \phi^m S_w^n, \tag{3}$$

where constants m (the cementation factor), a and n can be determined from reference samples or chosen according to published values for the respective sediment type. Typical values for marine sands are $m = 1.5 \quad 1.8$ and $a = 1$ (Evans, 2007). The pore water saturation factor S_w ($0 \le S_w \le 1$) is only relevant for marine sediments that include free gas or non-conducive fluids (Schwalenberg et al., 2010).

Sediment magnetic susceptibility κ_s depends primarily on magnetic mineral content, which is expressed by the porosity-independent matrix susceptibility κ_m of the sediment. However, κ_s bears also a dilution effect by porosity as shown by the equation

$$\kappa_s = (1 - \phi)\kappa_m + \phi\kappa_w, \tag{4}$$

with pore water susceptibility κ_w. By substituting equation 3 (solved for porosity ϕ) into equation 4, we can determine the apparent matrix susceptibility κ_m from the conductivity and susceptibility measurements to achieve the mineral specific, porosity-independent parameter. Matrix susceptibility can be used to separate provenance specific sediment properties against textural effects and susceptibility reduction due to a diagenetic overprint against dilution by increasing water content.

Representation of a homogenous subsurface

Although inappropriate for stratified marine deposits, the assumption of a homogeneous sediment half-space is decisive in defining fundamental constraints of EM signal formation. For this simple case, the conversion of secondary EM in-phase and quadrature components into susceptibility and conductivity data is realized by a look-up table, solving the Hankel transformation of the receiver function (equation 1) with coefficients given by Anderson (1979). Real (in-phase) and imaginary (quadrature) components of the secondary field can be used to determine subsurface conductivity provided that the conductivity of the upper half-space (i.e., seawater) is precisely known, in our case from synchronous CTD readings. The CTD point measurement is only representative, if bottom water conditions are nearly invariant within the sensing volume

of the CSEM sensor. Heterogeneous (e.g., freshwater plumes) or layered water masses (e.g., close to the thermocline or seasurface) give rise to systematic errors in the determination of subsurface conductivity.

Although layered water masses and a water-air boundary could be included in the 1D formulation of the receiver function (equation 1), GEM-3 measurements are only marginally influenced by the air boundary when working in water depths greater than 10 m (Figure 3). Obviously, water depth is not critical at all for susceptibility measurements, as the replacement of diamagnetic water by nonmagnetic air has just minute effects of $<4 \times 10^{-6}$ even for extremely shallow settings (e.g., in the surf zone). In contrast, the conductivity measurement is strongly affected in very shallow water depths. As shown by our model results, the required water depth to justify the assumption of homogenous seawater half-space crucially depends on operation frequency and phase. For our typically applied frequencies of 525, 2025, 4775, and 16,025 Hz, the respective critical minimum water depths are 6, 4, 3, and 2 m for quadrature conductivity and 12, 8, 5, and 3 m for in-phase conductivity.

As given by the resistive limit equation (equation 2), magnetic susceptibility can be exclusively determined from low frequency EM sounding. Figure 4a delineates the relative contribution of magnetic susceptibility to the in-phase signal as a function of transmitter frequency and sediment conductivity for a typical saltwater environment (modified after Won and Huang, 2004). Close to the resistive limit condition, the in-phase signal is almost purely controlled by magnetic susceptibility. Residual conductivity effects can be eliminated computationally or even neglected with little consequence. When measuring susceptibility at 75 Hz in seawater of 3 S/m over a subsurface with a conductivity of 1.2 S/m, less than 1% of a measured value of 100×10^{-6} is related to subsurface conductivity. Only for very weakly magnetic sediments with susceptibilities below 10×10^{-6}, neglecting conductivity compensation would significantly bias the susceptibility measurement. Hence, this figure specifies the operation frequencies that fulfill the resistive limit condition based on the expected range of susceptibility and conductivity values.

On the other hand, susceptibility has negligible effects on the determination of the quadrature conductivity of marine sediments (Huang and Won, 2003). The precision of the conductivity determination is, therefore, only related to the ambient EM noise floor. During static measurements on the sea bottom, noise was found to be less than 1 ppm for in-phase and quadrature components over the frequency range of 200 to 20,000 Hz. The conductivity equivalent of 1 ppm (noise floor) is shown in Figure 4b, assuming seawater and seafloor conductivities of 3 S/m and 1 S/m, respectively. At 5 kHz, we can assume a resolution of about 1 mS/m in quadrature and 8 mS/m in in-phase conductivity, corresponding to porosity changes of <0.1% and ca. 0.2%, respectively, while at 500 Hz resolution is 13 mS/m in quadrature and 205 mS/m in-phase conductivity equivalent to porosity variations of ca. 0.4% and 5.9%.

Representation of a heterogeneous subsurface

For typical coastal and continental shelf settings, the assumption of a homogenous seafloor is not adequate. Magnetic and electric properties of surficial sediments vary both in the vertical (e.g., by stratification, consolidation, diagenesis, free gas, freshwater aquifers) and in the horizontal dimension (e.g., lateral facies changes, point and line anomalies, seeps). In this section, we will

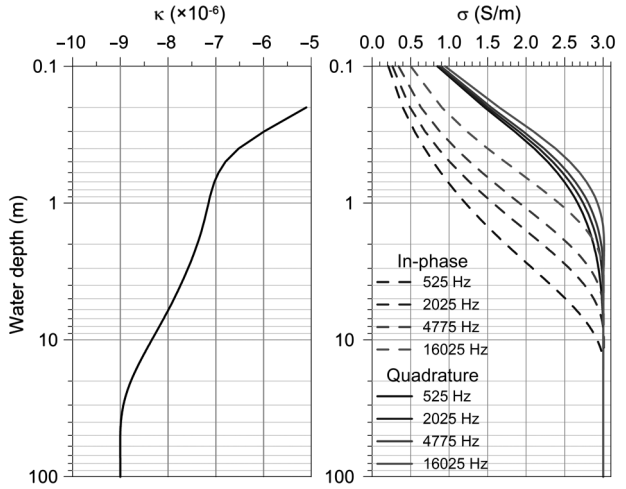

Figure 3. Modeled GEM-3 susceptibility and conductivity response under decreasing water depth. This model result assumes that the sensor emerges from an infinite seawater half-space ($\kappa_w = -9 \times 10^{-6}$ and $\sigma_w = 3$ S/m; susceptibility in SI-units).

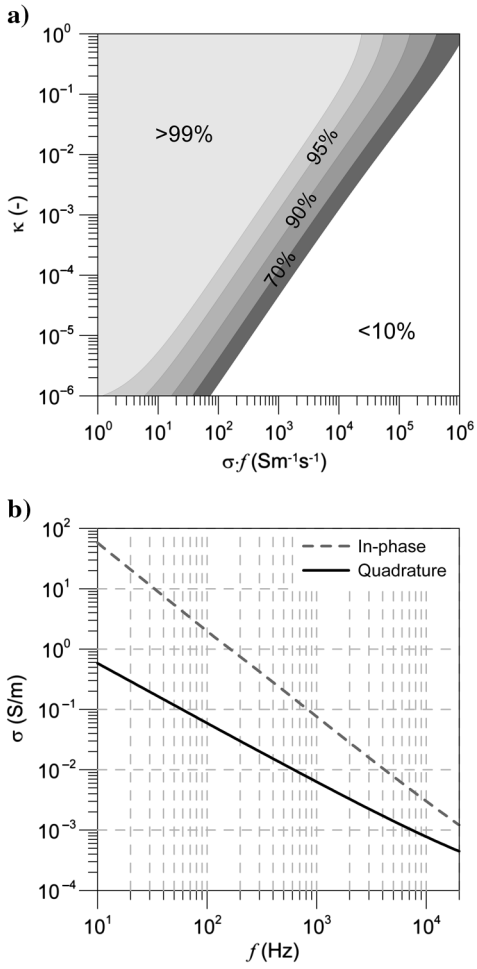

Figure 4. (a) Relative contribution of the magnetic (complementary to the electric) response to total in-phase signal in function of EM field frequency, sediment susceptibility and conductivity (modified after Won and Huang, 2004); (b) Frequency-dependence of in-phase and quadrature conductivity noise floor ($\sigma_w = 3$ S/m).

treat the two idealized cases of a vertically and a radially varying seafloor.

To calculate the EM response of a stratified subsurface of n layers, we extend the receiver function for a homogeneous subsurface (equation 1) to a vertically layered subsurface by substituting $\hat{Y}_s = \mu_w u_s$ against a recursive series (Ward and Hohmann, 1988)

$$\hat{Y}_k = Y_k \frac{\hat{Y}_{k+1} + Y_k \tanh(u_k h_k)}{Y_k + \hat{Y}_{k+1} \tanh(u_k h_k)}$$
$$\text{with} \quad Y_k = \frac{u_k}{i\omega\mu_0\mu_k}$$
$$\text{and} \quad u_k = \sqrt{\lambda^2 + i\omega\mu_0\mu_k\sigma_k}. \qquad (5)$$

Any layer k ($1 \le k < n$) is characterized by its relative magnetic permeability μ_k, electric conductivity σ_k and thickness h_k. The nth layer is given by $\hat{Y}_n = Y_n$ (Ward and Hohmann, 1988).

To model the response of the CSEM sensor to vertical susceptibility and conductivity distributions, respective sensor characteristics or "weighting functions" are required. Apparent seafloor conductivity and susceptibility values determined by EM profiling then correspond to a convolution of the vertical distribution function of these sediment properties and the respective weighting functions. Following Evans (2001), these functions were numerically determined by simulating a thin anomalous horizontal layer shifted vertically through a uniform sediment half-space. The lower half-space was discretized into layers of 1 mm, which were consecutively perturbed by 0.1% of their background value. The sensor's response to the ratio of the perturbed relative to the unperturbed model delineates its characteristic vertical distance sensitivity. To derive the weighting functions, the change in response was normalized, such that the integral over the entire sediment half-space equals one.

Figure 5a and 5b depicts the resulting weighting functions of in-phase susceptibility and quadrature conductivity modeled with a seawater conductivity of 3 S/m, sediment susceptibility of 100×10^{-6}, sediment conductivity of 1 S/m and sensor elevation of 0.2 m above seafloor. The cumulative curves quantify the contribution of the sediment volume between seafloor and a given depth plane to total sensor response.

The vertical characteristics for in-phase susceptibility and quadrature conductivity (5 kHz) differ mainly within the upper (seawater) half-space, while their decay within the sediment half-space is rather similar. The sensitivity to changes in conductivity (or susceptibility, respectively) reduces to 50% at a depth of 16 cm (17 cm) and to 10% at a depth of 71 cm (48 cm). In cumulative terms, the upper 0–21 cm (0–14 cm) of sediment corresponds to 50% and the upper 0–92 cm (0–50 cm) to 90% of the signal. If the sensor elevation falls below 0.13 m above seafloor, the susceptibility signal diminishes due to the increasing predominance of the magnetic inverse field of the bucking coil. The quadrature conductivity signal is not influenced by this bucking effect, but values would still decrease since bottom water is replaced by less conductive sediment.

The good geometric agreement of both sensor characteristics and, hence, investigated sediment volumes permits to combine in-phase susceptibility and quadrature conductivity values in interpretations and calculations. Frequency has no influence on the shape of the susceptibility response function and only little effect on the shape of the quadrature conductivity response function. On the contrary, the vertical characteristic of in-phase conductivity is substantially controlled by the operation frequency (Figure 5c) and is obviously beyond the sensitive area of the susceptibility signal.

In analogy to the definition of Liu and Becker (1990), the horizontal footprint of the secondary EM field (Figure 6) was

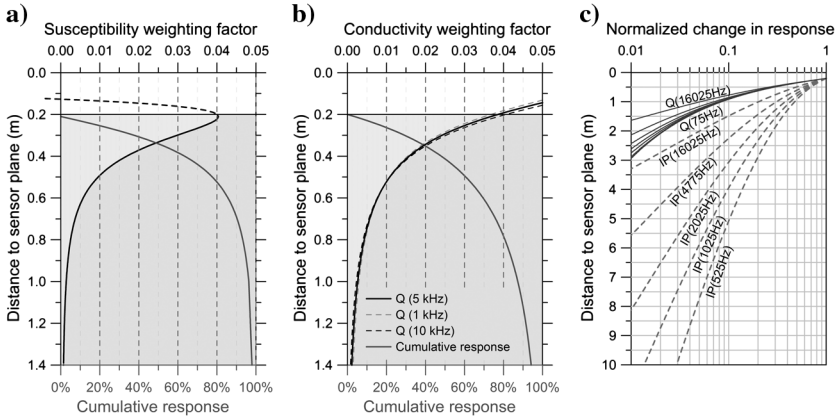

Figure 5. Vertical sensor characteristics of GEM-3 (96 cm coil) for (a) in-phase susceptibility and (b) quadrature conductivity given as weighting functions and cumulative subsurface response. (c) In-phase (IP) and quadrature (Q) responses of GEM-3 sensor at various operation frequencies. The models are based on 0.1% perturbations of an homogenous seafloor model with seawater (and sediment) conductivities/susceptibilities of 3 S/m and -9×10^{-6} (1 S/m and 100×10^{-6}; susceptibility in SI-units).

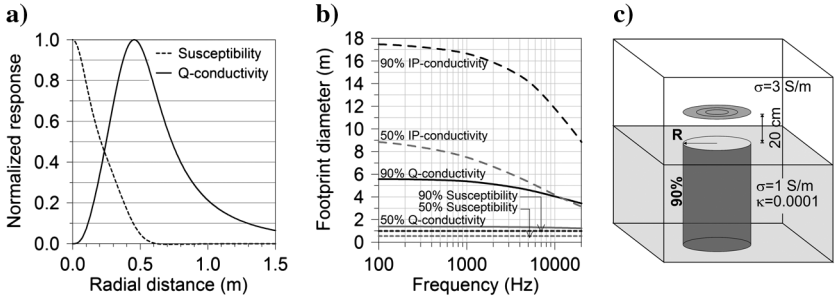

Figure 6. (a) Lateral response of GEM-3 sensor (96 cm coil) for susceptibility and 5 kHz quadrature conductivity on homogeneous seafloor normalized to peak values and (b) horizontal footprint diameter (90% of the total signal) and half-with (50%) of susceptibility, quadrature (Q) and in-phase (IP) conductivity; (c) model settings: sensor elevation 0.2 m, seawater (seafloor) susceptibility -9×10^{-6} (100×10^{-6}) and conductivity 3 S/m (1 S/m).

numerically calculated as the diameter of a semi-infinite cylinder that provides 90% of the total secondary signal with identical model settings. The primary electric field was determined by a finite-element model; Biot Savart's law was used to calculate the contribution of discrete rings (1 cm height, 1 cm width, and radius R) to the total secondary magnetic field at the center of the receiver coil. The footprint diameter for a given frequency and phase was determined by adding up the contributions of cylinder shells of infinite depth with increasing radii until 90% of the total signal were attained.

Simulations (Figures 5 and 6) demonstrate that the sensitive volumes of susceptibility and (in-phase and quadrature) conductivity differ more in the lateral than in the vertical dimension. Due to the dipolar shape of the magnetic and toroidal shape of the electric primary fields, sensitivity is highest near the coil axis for susceptibility and around the transmitter coil for quadrature conductivity (Figure 6a). The footprint of quadrature conductivity is 3.5 to 5.5 m and, therefore, considerably larger (half-width of 1.3 to 1.5 m) than that of susceptibility (1.0 m footprint and 0.5 m half-width). In the case of in-phase conductivity, the footprint is even wider (9 to 17 m; half-width of 3 to 9 m) due to lateral wave propagation (Figure 6b). The frequency dependence of footprint size has the potential for the coverage of offtrack conductive bodies (e.g., seeps, metal objects).

Combining all investigated aspects of sensing geometry as well as phase- and frequency-dependence, we can conclude, that

- Magnetic susceptibility is preferentially determined from the low frequency in-phase signal. Depth penetration is shallow (ca. 0.5 m) and essentially determined by sensor geometry.
- The 1–10 kHz quadrature conductivity signal provides the highest signal to noise (S/N) ratio, the highest lateral resolution and the best spatial compatibility with the susceptibility measurement.
- The 1–10 kHz in-phase conductivity signal has a wider footprint and deeper, frequency-dependent penetration, but a much lower S/N ratio than quadrature conductivity. It provides a means to map deeper strata, e.g., the thickness of mud layers or depth of erosional contacts.
- Under ideal conditions, the GEM-3 sensor can resolve susceptibility changes of 1×10^{-6} and conductivity changes of 1 mS/m (corresponding to a porosity change of 0.1%).

EM data collected at various frequencies, phases, and sensor diameters open interesting possibilities to determine vertical susceptibility and porosity transitions and gradients as demonstrated by the model examples of Figure 7: The first model (Figure 7a) represents a sand layer dipping below a muddy drape of higher susceptibility and conductivity. The sand facies contributes significantly to the magnetic susceptibility signal at a mud thickness < 1 m. In the 5 kHz quadrature conductivity signal the sand remains detectable under a mud cover of < 2.5 m (< 5 m at 0.5 kHz). The second model (Figure 7b) deals with the loss of magnetic susceptibility associated with pervasive magnetite dissolution (pyritization) in the sulfidic zone (e.g., Canfield and Berner, 1987). Magnetite depletion was assumed to set in at depths of 0.2–0.8 m and to be completed 0.2 m deeper. By combining various available GEM-3 sensor sizes (96, 64 and 40 cm), one could reasonably estimate the depth of the iron redox boundary.

BENTHIC EM PROFILER DESIGN AND OPERATION

As outlined in the previous chapters, the ground distance of the specified sensor is confined to 20 cm and should be maintained at a precision of ~1–2 cm. For a moving, continuously profiling system, such narrow tolerance in distance control can only be achieved with a bottom contact platform with excellent hydrodynamic and gliding properties, rigidity, and sufficient inert mass. The platform has to tolerate a tow line drag of up to three tons (load of rupture), withstand abrasive ground friction, and endure collisions with obstacles such as boulders, plant, and mussel cover, fishing gear or other manmade objects. It must protect the enclosed sensors and other electronic components from shock and silting up, while allowing free passage of the ambient bottom water. All structural parts should be nonconductive and nonmagnetic, hence nonmetallic, in order not

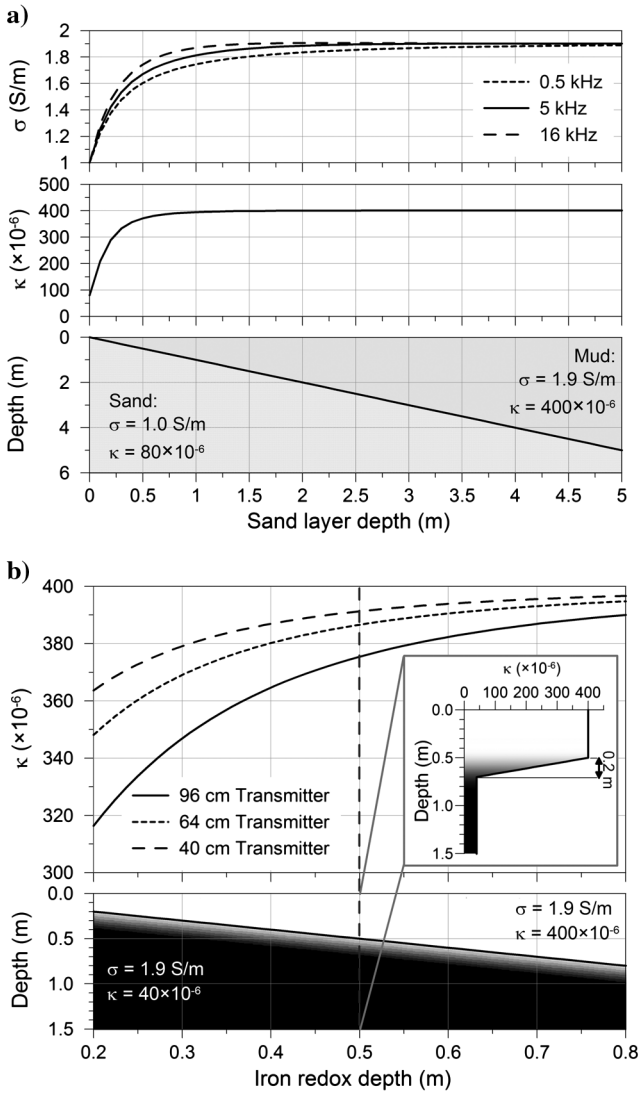

Figure 7. Simulations of (a) apparent susceptibility and conductivity profiles of a dipping mud/sand boundary (b) apparent susceptibility profiles by various available sensor sizes of dipping sulfidic (magnetite-reducing) zone (assumption: magnetite dissolution sets in at depths of 0.2–0.8 m and is completed 0.2 m deeper).

to bias or perturb the primary and secondary EM fields. To enable a wide range of coastal to open ocean survey concepts, the system should be operational with various ship classes (~10 to 100 m size), winches and cranes. Real time communication is of vital importance to permanently control the platform's motion (heading, water depth, roll and pitch, ground contact) and the quality of the acquired EM and hydrographic data.

The design of the Neridis II benthic EM profiler (Figure 8 and Table 1) accounts for all of the above requirements. The streamlined hull consists of two symmetric epoxy fiberglass/Kevlar shells with openings in front and stern providing a continuous flow-through of ambient water. A tapered concrete ram bow clears obstacles, absorbs shocks, and compensates the upward pull of the tow line. Three PVC skids (a central of 2.8 m and two lateral of 0.8 m length) provide a steady course (typically ±1°) and low pitch (±2°) and roll (±1°) angles. A stable dive and soft landing is achieved by adjusting winch slack to ship speed. Stable ground contact (zero pitch) can be maintained at tow speeds of 2–4 knots. The tow cable length is dynamically adjusted to about 3.5 times water depth. In the case of collision with large obstacles, a break point at the bow releases the tow cable. The profiler is then recovered by a trailed Kevlar safety line with head buoy.

The original GEM-3 CSEM sensor (Won et al., 1997) had to be adapted to underwater operation. Coils were wound onto a massive, pressure-resistant carrier disk and enclosed in a circular oil-filled PVC casing. All electronic units (console, embedded PC, DSL link, pitch and roll sensor with tilt-compensated 3-axial magnetometer) were installed in a semi-evacuated glass benthos sphere with five connectors. GEM-3 sensor, CTD, deep-sea battery, and pressure housing were attached to the hull via transverse, rubber-damped fiberglass profiles, keeping the distance between sensor head and electronics 1.2 m apart. High-speed data transmission (192 kbit/s to 2.3 Mbit/s) between profiler and tow ship was realized by 11 mm armored coax-cable and a SHDSL extender for 10/100BaseTX (Ethernet) networks.

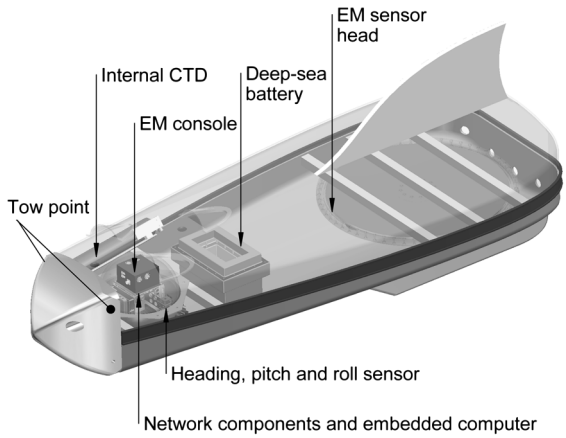

Figure 8. Virtual 3D view of Neridis II profiler (NERItic DIScoverer; lid shown transparent).

Table 1. Technical specifications of the Neridis II profiler.

Total dimensions	Length: 3.2 m, width: 1.2 m, height: 0.6 m (without fin)
Total weight	420 kg (in air), 120 kg (in water)
Transmitter moment	30 Am^2 peak (48 V/21 A)
Power	24VDC (deep-sea battery with 40 Ah)
Tow speed	2–4 knots
Tow cable length	3.5 times water depth (20° tow angle)
Sampling rate	EM (25 Hz), CTD (1 Hz), motion (5 Hz)
Mission duration	8 h (30 Am^2), 12 h (20 Am^2)

In-phase and quadrature components of the secondary EM fields are recorded at a sampling rate of 25 Hz for each of the frequencies in use (e.g., 75, 175, 525, 1025, and 4775 Hz). EM, CTD, and motion sensor are synchronized by the GPS time pulse (delay <100 µs), that is provided via the high-speed Ethernet link from the ship. The position of the profiler is determined from its heading and horizontal layback relative to the tow ship's DGPS position. All measurement, navigation and system status data are graphically and numerically displayed in real time.

During postprocessing, the hydrographic and navigation data are interpolated and resampled to a common clock. CSEM sensor intrinsic noise is filtered by applying a 5 Hz low-pass filter to in-phase and quadrature data. CTD conductivity is used to measure and correct bucking offset (zeroing) and drift of the CSEM sensor when the profiler is descending or ascending through the water column before and after each profile. The corrected EM data are converted to electric conductivity (4775 Hz quadrature) and magnetic susceptibility (75 Hz in-phase) with a look-up table method based on the receiver function (equation 1). The derived apparent conductivity value is used to subtract its potential contribution to the in-phase signal prior to susceptibility calculation.

APPLICATIONS IN COASTAL AND CONTINENTAL SHELF RESEARCH

As practical examples for CSEM surveying in coastal and continental shelf research, we present here some summarized results of our first marine surveys with the Neridis II benthic profiler. Ground truthing of the EM system was performed by correlation with core material during first trials in 2007, in the Ría de Vigo, a northwest Iberian estuary. Shelf data were collected off northwest Iberia in 2008. The first example addresses sediment distribution in transition regions of mud, siliciclastic sands, and glauconite sands across a 30 km wide section of the northwest Iberian continental shelf in water depths of 50–270 m. The second example from the same region takes a close-up at a 10 km wide bottom-current induced sand wave field on the outer shelf and investigates the relations of bedform morphology and sediment composition. A pilot study on sediment and scrap metal distribution in the Galician Ría de Vigo (Rey et al., 2008) and another, very detailed survey of groundwater seeps in Eckernförde Bay, western Baltic Sea (Müller et al., 2011) are published separately.

Ground truthing

For ground truthing the first measured in situ data, we compared porosity and susceptibility values from EM profiling and piston coring over a range of sandy to muddy sediments in the Ría de Vigo (Figure 9). Core lengths of 20 to 40 cm were taken with a piston

corer and subsampled at 2 cm intervals into 6.2 cm^2 plastic cubes. Sediment porosity was determined both from EM conductivity using Archie's law (equation 3 with $m = 1.6$ and $a = 1$) and from weight loss during the drying of the samples. Sediment susceptibility was measured with a laboratory susceptometer. Downcore data were averaged with the respective weighting functions (Figure 5a and 5b) to correspond to the EM data.

The apparent porosity and susceptibility values measured closest to the locations of the cores are in good agreement with the core values (Figure 9). Deviation from the linear regression curve is in the order of 1.0% (24×10^{-6}), i.e., well within the limits of analytics. A linear slope close to one demonstrates the reliability of EM derived susceptibility. Although regression through the origin is in both cases covered by the 95% confidence intervals, offsets of the regression curves could be also explained by imprecision of the sensor's elevation above seafloor. It is likely that the skids of the profiler carve a few centimeters into softer sediments. This would explain why some EM porosities appear lower and susceptibility 38×10^{-6} higher than predicted by the core material.

Sediment distribution on shelves

The northwest Iberian continental shelf (Figure 10b and 10c) is a high energy, low accumulation nonglaciated shelf of generally narrow width (25 to 50 km) with a large variety of sediment types and patterns (Dias et al., 2002a, 2002b; Lantzsch et al., 2009; Mohamed et al., 2010). EM profiling in this area had the objective to classify the facies and textures of the surficial sediments and to map their distribution at meter-scale spatial resolution with a special focus on transitions.

Four major sediment facies were defined from cored material (Odin and Lamboy, 1988; Lantzsch et al., 2010; Mohamed et al., 2010):

- The mud facies comprises fine-grained, mostly muddy Holocene high-stand sediments originating mainly from the Duero and Miño rivers and deposited in two successive coast-parallel mud belts of ~50 km length, 2–3 km width at water depths of 110–120 m (Figure 10c) by northward currents (Mohamed et al., 2010);
- The mixed sand facies consists of relict and reworked siliciclastic and carbonatic sands deposited at moderate hydrodynamic regimes (Lantzsch et al., 2010);
- The glaucony facies consists of mostly relict, late Miocene (5–6 Ma) sands containing up to 50% paramagnetic glaucony (Odin and Lamboy, 1988). This facies is indicative of slow to arrested sediment accumulation on the outer shelf;
- The gravel facies is dominated by bioclasts and siliciclasts (Odin and Lamboy, 1988) and represents low-stand shoreface and storm deposits.

Sediment composition of the outer shelf varies with supplied material, local hydrodynamic conditions and morphology. In particular, resuspended sediments from the mud patches are believed to be carried off the shelf when storm events coincide with downwelling conditions (Dias et al., 2002a). However, more than 70% of the modern sediments supplied to the Iberian margin are stored on the shelf (Jouanneau et al., 2002).

During *RV Poseidon* cruise P366/3 in 2008 on the northwest Iberian (Galician) shelf, more than 300 km total profile length was surveyed by means of the Neridis II benthic profiler during 11 successful 5–7 hour dives. The Galician mud belt was crossed at 41°45′ N and 42°10′ N by two east-west oriented EM profiles (Figure 10a and 10d) shown in compilation with the depth and salinity logs of the internal CTD and coincident boomer profiles collected by Hanebuth et al. (2007).

The boomer sections of the northern and southern profile (Figure 10a and 10d) depict the modern Galician mud belt as an up to 6 m thick stratified Holocene mud lens deposited on top of older transgressive sand deposits (Rey, 1993). In the EM profiles, the mud-belt is represented by concurrent, slightly asymmetric susceptibility and porosity highs. Confinement of mud and sand is most distinct in the southern profile (Figure 10d), where the shapes of susceptibility and porosity profiles closely reflect the distribution of silt and clay described by Dias et al. (2002b). Apparent magnetic susceptibility rises westward from 520 to 630 and back to 300×10^{-6}; apparent porosity rises from 59% to 63% and back to 53% along this track. The rising susceptibility and porosity values at the lateral transition from sand to mud facies could be explained in two ways: (1) by compositional changes and (2) by a two-phase model of increasing mud thickness (Figure 7a). Hence, 1D inversion, ideally with the aid of acoustic and sample-based data, is essential to exploit the full potential of the CSEM method.

The northern profile (Figure 10a) is more complex as it contains several sediment facies and bedforms on the inner and outer shelf. The apparent magnetic susceptibility increases from 490×10^{-6} at km 1 to 640×10^{-6} at km 6 of the profile and slightly decays to a local minimum at 580×10^{-6} at km 6.8, while apparent porosity rises from 58% in the east to 61% at km 5.2 and returns to 52%

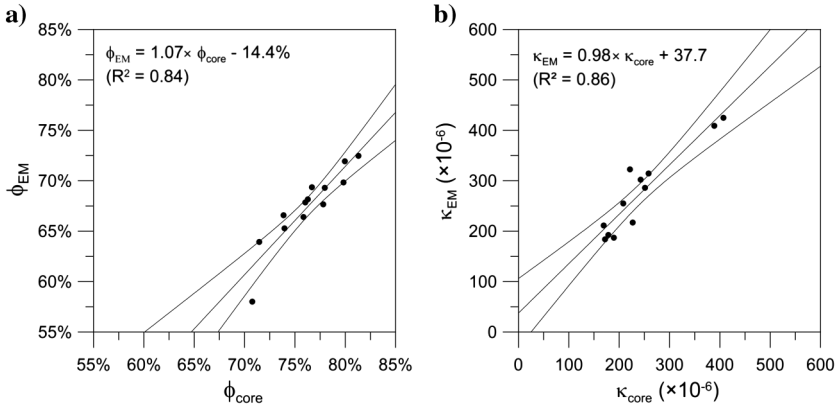

Figure 9. Correlation of EM and sediment core porosity and magnetic susceptibility (*dots*: mean of EM readings within 5 m radius of core location and weighted mean of core data; *lines*: linear trend and 95% confidence limits). EM Porosity is derived from Archie's law with constants $m = 1.6$ and $a = 1$.

at km 7. This structure corresponds to the mud-belt as shown by acoustics and suggested by Dias et al. (2002b) based on high silt and clay contents.

At water depths between 130 and 165 m (km 7 to 19), the profile transects a field of long wavelength bedforms documented by undulations in bathymetry as well as in susceptibility and porosity (see also the following chapter). Although the mean susceptibility of 660×10^{-6} in this section is as high as on the mud belt, a joint interpretation with relatively low porosity of about 46% clearly indicates poorly sorted glaucony sands (Figure 11). A material change to weakly magnetic, well sorted siliciclastic sands occurs west of km 19 in 160 to 175 m water depth. This section is characterized

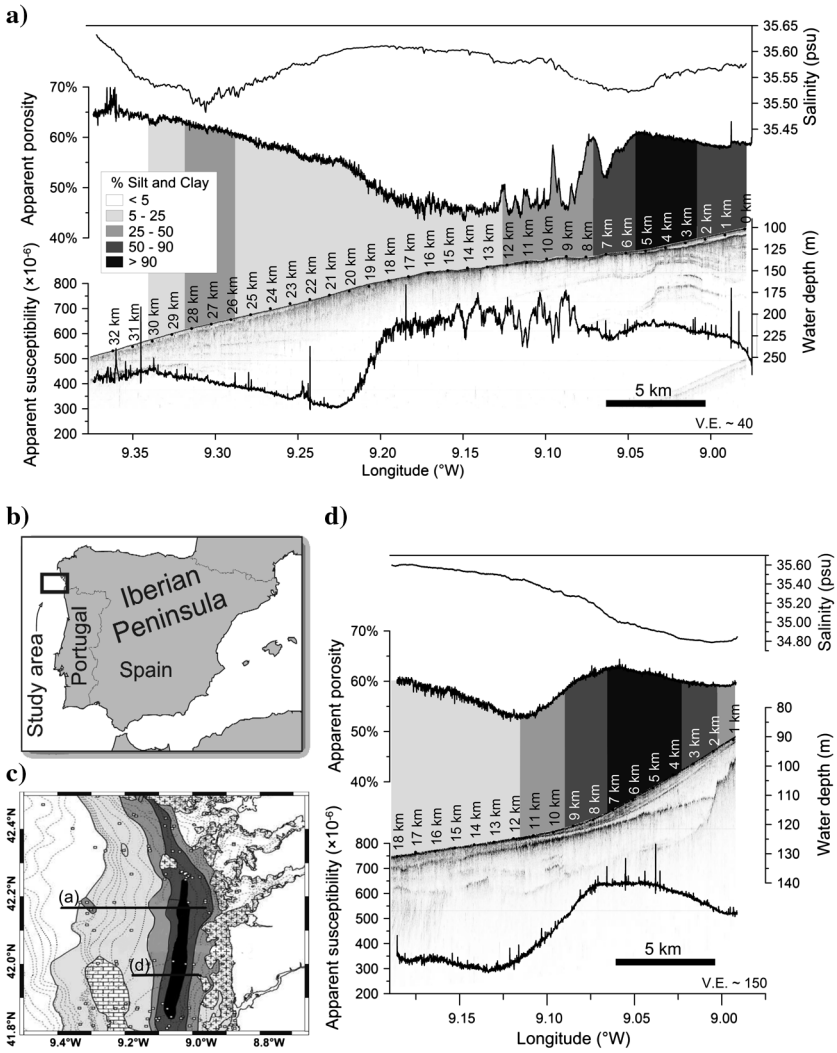

Figure 10. EM profiles GeoB-130,124 and 130,106 on the north-west Iberian Shelf. Parts (a) and (d) show CSEM-based porosity and magnetic susceptibility profiles in combination with CTD depth and salinity transects. Porosity is derived from Archie's law with constants $m = 1.6$, $a = 1$ and 14.4% offset (susceptibility with 37.7 offset; based on Figure 9). Acoustic boomer profiles by Hanebuth et al. (2007) delineate mud belt extension and bathymetry. Background colors show the sediment classification based on the silt and clay distribution map (c) according to Dias et al. (2002b).

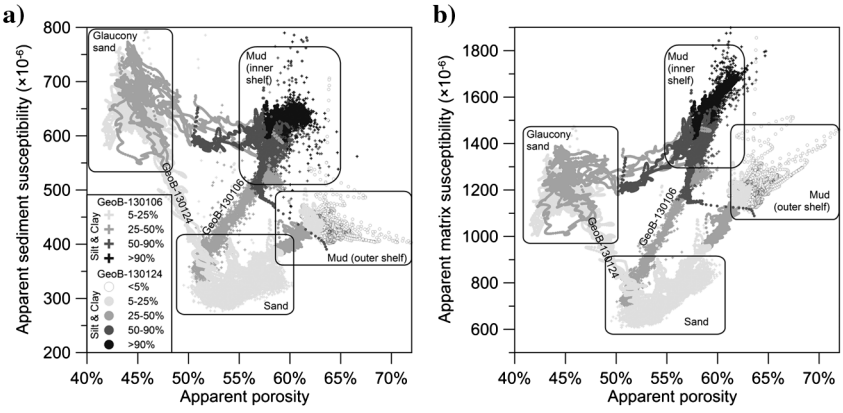

Figure 11. Main sediment facies (clusters) and transition zones (tracks) of EM profiles GeoB-130,124 and 130,106 visualized by combining susceptibility and conductivity data. Biplots of (a) sediment and (b) matrix susceptibility against porosity show the decisive influence of grain-size and compaction state on susceptibility.

by a boundary current system that causes strong to gradual winnowing of the fine fraction. The adjacent section of the outer shelf (km 26–30; >205 m water depth) is characterized by finer sediments and less saline bottom water.

Crossplots of sediment and matrix susceptibility against porosity demonstrate the petrophysical potential of EM sediment classification (Figure 11). The joint interpretation of both EM parameters allows distinct separation of the main sediment constituents given by the mud, glaucony, and sand facies as well as reworked and thereby magnetically reduced outer shelf deposits. Transitional environments between the sediment units cover several hundreds of meters within the profiles and are discriminative for facies end-members in the crossplots.

Bedforms

The EM measurements of the northern profile (Figure 10a) intersect the axis of coast parallel undulations (1–3 km in length, 0.5–2 m height) on the outer Galician shelf. As visible in the detailed section (Figure 12), local minimums in porosity and maxima in magnetic susceptibility coincide with local topographic highs. Porosity is 8%–12% lower than near the two easternmost ridges. The morphology of these ridges is almost symmetric although porosity shows steeper slopes at the eastern flanks. Comparable sand wave structures form by slope currents or internal waves where crests are oriented perpendicular to the main current direction (Hulscher, 1996). A ridge normal current will result in coarser and better sorted sediments on the upstream flank (e.g., Smith, 1969; Swift and Freeland, 1978) and finer-grained material on the downstream flank unless the winnowed sediments are transported out of the region. The asymmetry of the porosity indicates a westward current, which corresponds to storm driven downwelling in this area (Dias et al., 2002a). The magnetic susceptibility signal generally mirrors the porosity undulation. This finding is contrary to the relations of porosity, susceptibility, and grain-size observed in the southern profile (Figure 10d) and indicates that glaucony concentration is enhanced on the crests of the sediment waves.

The general structure of the major sediment waves is overlain by ridges of smaller wavelength and amplitude, showing a complex pattern of local deposition (preferably on western flanks: 11.8 km) and erosion. The relationship of morphology, porosity, and susceptibility terminates below 145 m water depth in the western part of the section.

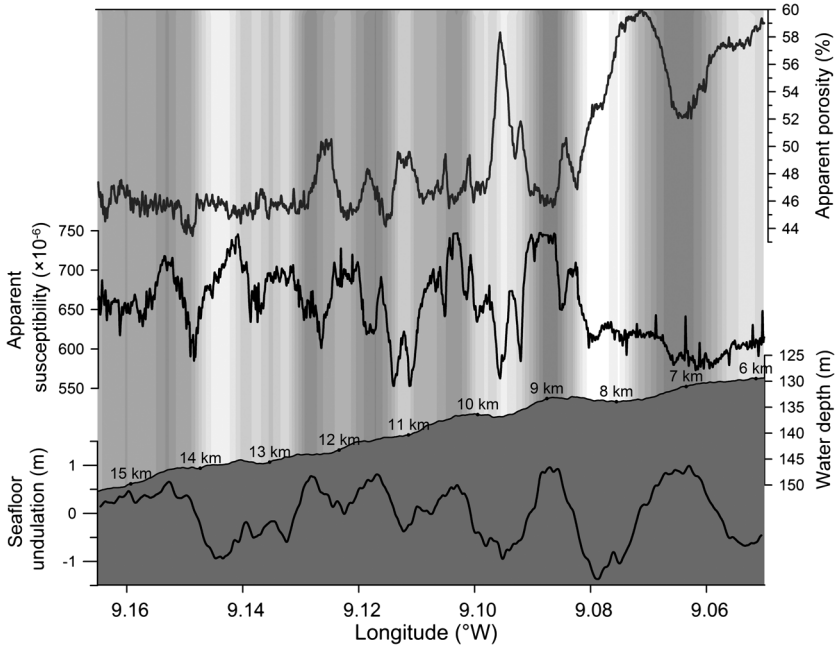

Figure 12. Sediment wave section of the northern profile (Figure 11a). The seafloor undulation parameter is derived by high pass filtering (3 km cut off) bathymetry and gives background colors (dark: crest, bright: valley).

CONCLUSIONS

Our theoretical derivations and models as well as practical implementations demonstrate that benthic EM profiling with multifrequency concentric loop CSEM sensors is a very efficient and well interpretable new method to measure and map the electric conductivity and magnetic susceptibility of shallow marine surficial sediments. The sensitivity of the here presented system compares with standard laboratory instruments and is adequate to detect subtle changes in sediment composition related to petrology, redox state, grain-size, porosity, porewater salinity, and stratification at submeter lateral resolution.

The following key findings and solutions were made:

- Local bottom-water conductivity required for sensor calibration is measured by an internal oceanographic CTD;
- Sediment magnetic susceptibility is preferentially derived from low frequency (< 100 Hz) in-phase CSEM soundings;
- Sediment electric conductivity can be determined both from quadrature or in-phase CSEM soundings at higher frequencies (1–10 kHz); however, the first approach provides better sensitivity and a much smaller sensing volume, which compares better with the magnetic measurement;
- A sensor elevation of ~20 cm above the seafloor must be maintained within narrow limits to provide the best match of sensing volume and subsurface. This is a critical issue for free-floating sensor platforms (e.g., ROVs, AUVs) and our argument to opt for a bottom-towed benthic profiler.

Uncertainties regarding the intrinsic nature of electric and magnetic property changes are greatly reduced by the coincident detection and joint interpretation of both parameters. Bivariate plots of EM susceptibility versus conductivity data show great potential to differentiate the main lithologic units and delineate the diagenetic impact on iron minerals. Nevertheless, representative pre- and postsurvey sediment probing for sedimentological, geophysical, and geochemical laboratory analyses remains essential to refine and ascertain a regional interpretation scheme for EM survey data.

The narrow footprint, high sampling rate, and fair tow speed of the Neridis II system permit to cover and resolve sediment patterns of very different lateral extent from submeter (e.g., iron sulfide nodules, UXO) to kilometer scales

(e.g., drift bodies, placer deposits) within a single survey operation. Benthic EM profiling ideally complements hydroacoustic and hydrographic surveys by adding quantitative and comparative proxy information on the porosity and petrology of the shallow subsurface and by delineating the heterogeneity and distribution of littoral and neritic sedimentary facies.

ACKNOWLEDGMENTS

Our special appreciation goes to our coauthor Bill SanFilipo who passed away while the manuscript was in a very early stage. His theoretical contribution and advices formed the backbone of the system development and modeling.

The authors would like to thank I. J. Won, S. J. Norton, F. Funak, and A. Oren of Geophex Ltd. for great cooperation and support. We also thank T. Frederichs (MARUM) and F. Vilas and A. Andrade (GEOMA) for continuous assistance in the development process. The authors would like to thank Kerry Key for the detailed revision and great support to develop equation 1 in such a beautiful way that improved this manuscript substantially. We further thank M. A. Vallée and two anonymous reviewers as well as the editors for constructive criticism and helpful comments. Special thanks go to K. Schwalenberg for helpful discussions and comments and N. Gehlen for assistance in the manufacturing process. Many thanks go to the crew of RV Poseidon cruise P366/3. Development and implementation of the electromagnetic benthic profiler Neridis II was jointly funded by MARUM incentive funding and two research grants of the Marine and Environmental Geology Group (GEOMA) at the University of Vigo (Spain), PGDIT06-TAM31201PR (XUGA) and CTM 2007-61227/MAR (MICINN). H. Müller and C. Hilgenfeldt were funded through DFG-Research Center/Cluster of Excellence "The Ocean in the Earth System." This work is part of MARUM projects C1 and SD2 investigating sediment dynamics at ocean margins.

APPENDIX A

THEORETICAL RESPONSE OF THE COINCIDENT COIL SENSOR FOR A HOMOGENEOUS SUBSURFACE

Consider a horizontal circular transmitter coil T_x with radius R_t and number of turn n_t and a concentric coaxial bucking coil B_x with radius R_b and number of turn n_b, both excited by current I but with opposed polarity and situated at height h above the seafloor. Starting from equation 4.88 given by Ward and Hohmann (1988, page 219), we can write out the expression of the vertical magnetic field recorded by the sensor, as

$$H_z(r) = \frac{I}{2}\int_0^\infty (n_t R_t J_1(\lambda R_t) - n_b R_b J_1(\lambda R_b)) \\ (r_{TE} e^{-2u_w h} + 1)\frac{\lambda^2}{u_w} J_0(\lambda r)\mathrm{d}\lambda, \tag{A-1}$$

with the *reflection coefficient* $r_{TE} = \frac{\mu_s u_w - \mu_w u_s}{\mu_s u_w + \mu_w u_s}$, where

$$u_w = \sqrt{\lambda^2 + i\omega\mu_0\mu_w\sigma_w} \quad \text{and} \quad u_s = \sqrt{\lambda^2 + i\omega\mu_0\mu_s\sigma_s}.$$

Therein, σ_s (σ_w) is the electric conductivity of the sediment (seawater), μ_s (μ_w) is the relative magnetic permeability of the sediment (seawater), μ_0 the magnetic permeability of free space, J_1 the Bessel function of first kind and order, i the imaginary number, and ω the angular frequency ($\omega = 2\pi f$; f: frequency).

At the center of the coils $r = 0$ and $J_0(0) = 1$, we then have

$$H_z(r=0) = \frac{I}{2}\int_0^\infty (n_t R_t J_1(\lambda R_t) - n_b R_b J_1(\lambda R_b)) \\ (r_{TE} e^{-2u_w h} + 1)\frac{\lambda^2}{u_w}\mathrm{d}\lambda. \tag{A-2}$$

A scattered field is produced when the seafloor has a different conductivity or permeability than the seawater. This term is associated with reflection coefficient r_{TE} in equation A-2 and the scattered magnetic field within the receiver coil (approximated to be uniform rather than having r dependence) can be separated to

$$H_z^s(r=0) = \frac{I}{2}\int_0^\infty (n_t R_t J_1(\lambda R_t) \\ - n_b R_b J_1(\lambda R_b))(r_{TE} e^{-2u_w h})\frac{\lambda^2}{u_w}\mathrm{d}\lambda. \tag{A-3}$$

The response of the sensor is given by the ratio of the secondary magnetic field to the primary field of the transmitter coil in parts per million (ppm). We simplify the primary field to a simple geometric field, making use of the approximation that $\lambda/u_w \approx 1$. In equation A-2, the primary field produced by the transmitter coil is then

$$H_{z,Tx}^p = \frac{I}{2}\int_0^\infty n_t R_t J_1(\lambda R_t)\frac{\lambda^2}{u_w}\mathrm{d}\lambda \approx \frac{n_t I}{2R_t}. \tag{A-4}$$

The voltage V induced in a horizontal receiver coil of radius R_r placed in the center of the transmitter and bucking coils is proportional to the time derivative of the magnetic flux passing through the receiver loop. From Ward and Hohmann (1988, p221), we can write

$$V = -i\omega\mu\int_0^{R_r}\int_0^{2\pi} H_z(r) r\mathrm{d}\phi\mathrm{d}r. \tag{A-5}$$

Given the radial symmetry of H_z, the azimuthal integral simplifies to a factor of 2π. Using the Bessel function integral relation given in Ward and Hohmann (1988)

$$\int x^n J_{n-1}(x)\mathrm{d}x = x^n J_n(x) \tag{A-6}$$

and the substitutions $x = \lambda r$ and $dx = \lambda dr$ we can write

$$V = -i\omega\mu\pi I R_r \int_0^\infty (n_t R_t J_1(\lambda R_t) \\ - n_b R_b J_1(\lambda R_b))(r_{TE} e^{-2u_w h} + 1)\frac{\lambda}{u_w} J_1(\lambda R_r)\mathrm{d}\lambda. \tag{A-7}$$

From equations A-4 and A-5, the primary induced voltage is therefore

$$V_P = -i\omega\mu\pi\frac{n_t I R_r^2}{2R_t} \tag{A-8}$$

The normalized receiver response U is then V divided by V_P

$$U = \frac{2R_t^2}{R_r}\int_0^\infty G(r_{TE}e^{-2u_w h}+1)\frac{\lambda}{u_w}\mathrm{d}\lambda, \qquad \text{(A-9)}$$

with

$$G = \left(J_1(\lambda R_t) - \frac{n_b R_b}{n_t R_t}J_1(\lambda R_b)\right)J_1(\lambda R_r). \qquad \text{(A-10)}$$

We can then break this equation into a scattered term U_0 and a primary term U_1

$$U = U_0 + U_1, \qquad \text{(A-11)}$$

where

$$U_0 = \frac{2R_t^2}{R_r}\int_0^\infty G r_{TE}e^{-2u_w h}\frac{\lambda}{u_w}\mathrm{d}\lambda \qquad \text{(A-12)}$$

and

$$U_1 = \frac{2R_t^2}{R_r}\int_0^\infty G\frac{\lambda}{u_w}\mathrm{d}\lambda. \qquad \text{(A-13)}$$

The bucking principle of the GEM-3 efficiently removes primary field components from the received signal. However, imperfect bucking causes a certain bucking offset which is static in air and factory determined. From equation A-13, the bucking offset in air ($\lambda/u_w \approx 1$) is

$$U_b = \frac{2R_t^2}{R_r}\int_0^\infty G\mathrm{d}\lambda. \qquad \text{(A-14)}$$

The total response of the GEM-3 sensor above a homogenous subsurface (equation 1 is therefore derived by the sum of the scattered term U_0 and the difference of the primary terms $U_1 - U_b$

$$U = U_0 + (U_1 - U_b). \qquad \text{(A-15)}$$

REFERENCES

Anderson, W. L., 1979, Numerical integration of related Hankel transforms of orders 0 and 1 by adaptive digital filtering: Geophysics, **44**, 1287–1305, doi: 10.1190/1.1441007.

Archie, G. E., 1942, The electrical resistivity log as an aid in determining some reservoir characteristics: Journal of Petroleum Technology, **5**, 1–8.

Benech, C., and E. Marmet, 1999, Optimum depth of investigation and conductivity response rejection of the different electromagnetic devices measuring apparent magnetic susceptibility: Archaeological Prospection, **6**, no. 1, 31–45, doi: 10.1002/(SICI)1099-0763(199906)6:2<123::AID-ARP129>3.0.CO;2-N.

Booth, C. A., J. Walden, A. Neal, and J. P. Smith, 2005, Use of mineral magnetic concentration data as a particle size proxy: A case study using marine, estuarine and fluvial sediments in the Carmarthen Bay area, South Wales, U.K.: Science of the Total Environment, **347**, no. 1-3, 241–253, doi: 10.1016/j.scitotenv.2004.12.042.

Buselli, G., 1982, The effect of near-surface superparamagnetic material on electromagnetic measurements: Geophysics, **47**, 1315–1324, doi: 10.1190/1.1441392.

Canfield, D. A., and R. A. Berner, 1987, Dissolution and pyritization of magnetite in anoxic marine sediments: Geochimica et Cosmochimica Acta, **51**, no. 3, 645–659, doi: 10.1016/0016-7037(87)90076-7.

Chave, A. D., S. C. Constable, and R. N. Edwards, 1991, Electrical exploration methods for the seafloor, *in* M.N. Nabighian, ed., Electromagnetic methods vol. 2: Applications,931–966.

Cheesman, S. J., R. N. Edwards, and A. D. Chave, 1987, On the theory of seafloor conductivity mapping using transient electromagnetic systems: Geophysics, **52**, 204–217, doi: 10.1190/1.1442296.

Collinson, D. W., 1983, Methods in rock magnetism and palaeomagnetism: Chapman Hall.

Dearing, J. A., R. J. L. Dann, K. Hay, J. A. Lees, P. J. Loveland, B. A. Maher, and K. O'Grady, 1996, Frequency-dependent susceptibility measurements of environmental materials: Geophysical Journal International, **124**, 228–240, doi: 10.1111/gji.1996.124.issue-1.

De Meijer, R. J., I. C. Tánczos, and C. Stapel, 1996, Radiometry as a technique for use in coastal research, *in* M. de Batist, and P. Jacobs, eds., From geology of siliciclastic shelf seas: Geological Society Special Publication, **117**, 289–297.

Dias, J. M. A., R. Gonzalez, C. Garcia, and V. Diaz-del-Rio, 2002b, Sediment distribution patterns on the Galicia-Minho continental shelf: Progress in Oceanography, **52**, no. 2-4, 215–231, doi: 10.1016/S0079-6611(02)00007-1.

Dias, J. M. A., J. M. Jouanneau, R. Gonzalez, M. F. Araújo, T. Drago, C. Garcia, A. Oliveira, A. Rodrigues, J. Vitorino, and O. Weber, 2002a, Present day sedimentary processes on the northern Iberian shelf: Progress in Oceanography, **52**, no. 2-4, 249–259, doi: 10.1016/S0079-6611(02)00009-5.

Edwards, R. N., 2005, Marine controlled source electromagnetics: Principles, methodologies, future commercial applications: Surveys in Geophysics, **26**, 675–700.

Ellwood, B. B., W. L. Balsam, and H. H. Roberts, 2006, Gulf of Mexico sediment sources and sediment transport trends from magnetic susceptibility measurements of surface samples: Marine Geology, **230**, no. 3-4, 237–248, doi: 10.1016/j.margeo.2006.05.008.

Emiroglu, S., N. Petersen, and D. Rey, 2004, Magnetic properties of sediment in the Ría de Arousa (Spain): Dissolution of iron oxides and formation of iron sulphides: Physics and Chemistry of the Earth, **29**, no. 13-14, 947–959, doi: 10.1016/j.pce.2004.03.012.

Evans, R. L., 2001, Measuring the shallow porosity structure of sediments on the continental shelf: A comparison of an electromagnetic approach with cores and acoustic backscatter: Journal of Geophysical Research, **106**, 27047–27060, doi: 10.1029/2000JC000487.

Evans, R. L., 2007, Using CSEM techniques to map the shallow section of seafloor: From the coastline to the edges of the continental slope: Geophysics, **72**, no. 2, WA105–WA116, doi: 10.1190/1.2434798.

Gay, S. P., 2004, Glacial till: A troublesome source of near-surface magnetic anomalies: The Leading Edge, **23**, 542–547, doi: 10.1190/1.1766241.

Hanebuth, T., V. Bender, S. Bujan, M. Elvert, T. Frederichs, B. Kockisch, S. Krastel-Gudegast, H. Lantzsch, Á. Mena Rodríguez, F. Schmidt, F. Strozyk, and M. Wagner Friedrichs, 2007, Report and first results of the Poseidon cruise P342 GALIOMAR, Vigo-Lisboa (Portugal). Distribution pattern, residence times and export of sediments on the pleistocene/holocene Galician Shelf (NW Iberian Peninsula): Berichte, Fachbereich Geowissenschaften, University of Bremen, 255.

Hatfield, R. G., and B. A. Maher, 2009, Fingerprinting upland sediment sources: Particle size-specific magnetic linkages between soils, lake and suspended sediments: Earth Surface Processes and Landforms, **34**, June1359–1373, doi: 10.1002/esp.v34:10.

Huang, H., and I. J. Won, 2003, Detecting metal objects in magnetic environments using a broadband electromagnetic method: Geophysics, **68**, 1877–1887, doi: 10.1190/1.1635040.

Hulscher, S. J. M. H., 1996, Tidal induced large-scale regular bed form patterns in a three-dimensional shallow water model: Journal of Geophysical Research, **101**, 20727–20744, doi: 10.1029/96JC01662.

Jackson, P. D., D. Taylor Smith, and P. N. Stanford, 1978, Resistivity-porosity-particle shape relationships for marine sands: Geophysics, **43**, 1250–1268, doi: 10.1190/1.1440891.

Jouanneau, J. M., O. Weber, T. Drago, A. Rodrigues, A. Oliveira, J. M. A. Dias, C. Garcia, S. Schmidt, and J. L. Reyss, 2002, Recent sedimentation and sedimentary budgets on the western Iberian shelf: Progress in Oceanography, **52**, no. 2-4, 261–275, doi: 10.1016/S0079-6611(02)00010-1.

Kenny, A. J., I. Cato, M. Desprez, G. Fader, R. T. E. Schüttenhelm, and J. Side, 2003, An overview of seabed-mapping technologies in the context of marine habitat classification: Journal of Marine Science, **60**, no. 3, 411–418.

Lantzsch, H., T. Hanebuth, and V. B. Bender, 2009, Holocene evolution of mud depocentres on a high-energy, low-accumulation shelf (NW Iberia): Quaternary Research, **72**, no. 3, 325–336, doi: 10.1016/j.yqres.2009.07.009.

Lantzsch, H., T. Hanebuth, and R. Henrich, 2010, Sediment recycling and adjustment of deposition during deglacial drowning of a low-accumulation shelf (NW Iberia): Continental Shelf Research, **30**, no. 15, 1665–1679, doi: 10.1016/j.csr.2010.06.013.

Liu, G., and A. Becker, 1990, Two-dimensional mapping of sea ice keels with airborne electromagnetics: Geophysics, **55**, 239–248, doi: 10.1190/1.1442832.

Maher, B. A., S. J. Watkins, G. Brunskill, J. Alexander, and C. R. Fielding, 2009, Sediment provenance in a tropical fluvial and marine context by magnetic 'fingerprinting' of transportable sand fractions: Sedimentology, **56**, 841–861, doi: 10.1111/sed.2009.56.issue-3.

Manoj, C., A. Kuvshinov, S. Maus, and H. Lühr, 2006, Ocean circulation generated magnetic signals: Earth, Planets and Space, **58**, no. 4, 429–437.

Mohamed, K., D. Rey, B. Rubio, F. Vilas, and T. Frederichs, 2010, Interplay between detrital and diagenetic processes since the LGM on the NW Iberian continental shelf: Quaternary Research, **73**, no. 3, 507–520, doi: 10.1016/j.yqres.2010.02.003.

Müller, H., T. von Dobeneck, W. Nehmiz, and K. Hamer, 2011, Near-surface electromagnetic, rock magnetic, and geochemical fingerprinting of submarine freshwater seepage at Eckernförde Bay (SW Baltic Sea): Geo-Marine Letters, **31**, no. 2, 123–140, doi: 10.1007/s00367-010-0220-0.

Odin, G. S., and M. Lamboy, 1988, Glaucony from the margin off northwestern Spain, *in* G. S. Odin, ed., Green marine clays: Elsevier Science, **45**, 249–275.

Oldfield, F., B. A. Maher, J. Donoghue, and J. Pierce, 1985, Particle-size related, mineral magnetic source sediment linkages in the Rhode River catchment, Maryland, USA: Journal of the Geological Society of London, **142**, no. 6, 1035–1046, doi: 10.1144/gsjgs.142.6.1035.

Rey, D., K. J. Mohamed, A. Bernabeu, B. Rubio, and F. Vilas, 2005, Early diagenesis of magnetic minerals in marine transitional environments: Geochemical signatures of hydrodynamic forcing: Marine Geology, **215**, no. 3-4, 215–236, doi: 10.1016/j.margeo.2004.12.001.

Rey, D., H. Müller, B. Rubio, T. von Dobeneck, F. Vilas, C. Hilgenfeldt, T. Frederichs, A. Bernabeu, S. Fernandez, and K. J. Mohamed, and Grupo GEOMA, 2008, Using electromagnetic sensors to estimate physical properties and environmental quality of surface sediments in the marine environment. Preliminary results: Geotemas, **10**, 651–654.

Rey Salgado, J., 1993, Relación morfosedimentaria entre la plataforma continental de galicia y las rías bajas y su evolución durante el cuaternario: Publicaciones Especiales, Instituto Español de Oceanografía **17**, 1–233.

Schwalenberg, K., M. Haeckel, J. Poort, and M. Jegen, 2010, Evaluation of gas hydrate deposits in an active seep area using marine controlled source electromagnetics: Results from Opouawe Bank, Hikurangi Margin, New Zealand: Marine Geology, **272**, no. 1-4, 79–88, doi: 10.1016/j.margeo.2009.07.006.

Smith, J. D., 1969, Geomorphology of a sand ridge: Journal of Geology, **77**, 39–55, doi: 10.1086/jg.1969.77.issue-1.

Swift, D. J. P., and G. L. Freeland, 1978, Current lineations and sand waves on the inner shelf, middle Atlantic bight of North America: Journal of Sedimentary Petrology, **48**, no. 4, 1257–1266.

Tribovillard, N., O. Averbuch, A. Bialkowski, and J. F. Deconinck, 2002, Early diagenesis of marine organic-matter and magnetic properties of sedimentary rocks: The role of iron limitation and organic-matter source organisms: Bulletin de la Societe Geologique de France, **173**, no. 4, 295–306, doi: 10.2113/173.4.295.

van Wijngaarden, M., L. B. Venema, and R. J. De Meijer, 2002, Radiometric sand mud characterisation in the Rhine-Meuse estuary part b. In situ mapping: Geomorphology, **43**, no. 1-2, 103–116.

Ward, S. H., and G. W. Hohmann, 1988, Electromagnetic theory for geophysical applications, *in* M. N. Nabighian, ed., Electromagnetic methods in applied geophysics, SEG, 130–311.

Won, I. J., and H. Huang, 2004, Magnetometers and electro-magnetometers: The Leading Edge, **23**, 448–451, doi: 10.1190/1.1756834.

Won, I. J., D. A. Keiswetter, G. R. A. Fields, and L. C. Sutton, 1996, GEM-2: A new multifrequency electromagnetic sensor: Journal of Environmental and Engineering Geophysics, **1**, no. 2, 129–138, doi: 10.4133/JEEG1.2.129.

Won, I. J., D. A. Keiswetter, D. R. Hanson, E. Novikova, and T. M. Hall, 1997, GEM-3: A monostatic broadband electromagnetic induction sensor: Journal of Environmental and Engineering Geophysics, **2**, no. 1, 53–64, doi: 10.4133/JEEG2.1.53.

Yilmaz, O., 1987, Seismic data processing, *in* S. M. Doherty, and E. B. Neitzel, series ed., Investigations in geophysics 2, SEG.

Zhang, W., L. Yu, and S. M. Hutchinson, 2001, Diagenesis of magnetic minerals in the intertidal sediments of the Yangtze Estuary, China, and its environmental significance: Science of the Total Environment, **266**, no. 1-3, 169–175, doi: 10.1016/S0048-9697(00)00735-X.

Zhang, Z., and D. W. Oldenburg, 1997, Recovering magnetic susceptibility from electromagnetic data over a one-dimensional earth: Geophysical Journal International, **130**, 422–434, doi: 10.1111/gji.1997.130.issue-2.